

1 **Revision1**

2 **Liquid properties in the Fe-FeS system under moderate pressure: tool box to model**
3 **small planetary cores**

4 Guillaume Morard¹, Johann Bouchet², Attilio Rivoldini³, Daniele Antonangeli¹, Mathilde
5 Roberge¹, Eglantine Boulard¹, Adrien Denoeud⁴, Mohamed Mezouar⁵

6 ¹*Institut de Minéralogie, de Physique des Matériaux, et de Cosmochimie (IMPMC), Sorbonne*
7 *Universités - UPMC, UMR CNRS 7590, Muséum National d'Histoire Naturelle, IRD UMR*
8 *206, F-75005 Paris, France.*

9 ²*CEA, DAM, 91297 Arpajon, France*

10 ³*Royal Observatory of Belgium; B-1180 Bruxelles Belgium*

11 ⁴*Ecole Polytechnique, LULI, F-91128 Palaiseau, France*

12 ⁵*European Synchrotron Radiation Facility, Grenoble F-38043 France*
13

14 **Abstract**

15 **Physical properties of liquid Fe-S alloys (from 10 to 50 at%S) under high**
16 **pressure were investigated by in situ X-ray diffraction (up to 5GPa and 1900 K) and by**
17 **ab initio calculations. The local structure of Fe-S liquid alloys clearly show how S**
18 **modifies the local arrangement of the Fe atoms. Density has been extracted from the**
19 **diffuse scattering by minimization of the oscillation in the short distance of the radial**
20 **distribution function $g(r)$. Two different formalisms for the P-V-T-X equation of state**
21 **are presented in order to model density and sound velocity as a function of pressure,**
22 **temperature and sulfur content. Based on these results, Moon's core composition is**
23 **discussed. This coherent dataset will serve as a thermodynamically consistent ground for**
24 **modeling the core of small telluric planets and large icy satellites.**

25

26

27

28 Introduction

29 Elements lighter than iron are expected to be present in planetary cores, due to their
30 abundance in iron meteorites and their affinity with the metallic phase. Among the potential
31 light elements (Poirier 1994), sulphur is likely the most abundant in the cores of iron
32 meteorites parent bodies (Chabot 2004). From tungsten isotopes data (Kleine et al. 2009) and
33 experimental studies of percolation processes (Yoshino et al. 2003), core formation is
34 expected to occur within a few million years of the solar system formation, even in small
35 planetesimals (Greenwood et al. 2006). It is therefore important to constrain physical
36 properties of Fe-S liquid alloys in order to better understand core formation in the early stage
37 of the solar system.

38 Melting properties in the Fe-FeS system under high pressure have been intensively
39 investigated by *in situ* (Campbell et al. 2007; Morard et al. 2007b; Chen et al. 2008a; G.
40 Morard et al. 2008; Andrault et al. 2009) or *ex situ* methods (Chudinovskikh and Boehler
41 2007; Stewart et al. 2007; Chen et al. 2008b; Kamada et al. 2012). However, while the Fe-rich
42 side of the phase diagram begins to be relatively well described, we still lack precise
43 knowledge of important physical properties, especially in the liquid state, such as density or
44 viscosity (LeBlanc and Secco 1996; Sanloup et al. 2000; Vočadlo et al. 2000; Balog et al.
45 2003; Nishida et al. 2008).

46 As today, the inner structures and in particular the cores of planetary bodies in the Solar
47 system are not well known, mostly because of the absence of seismological data, with the
48 clear exception for the Earth and, to some extent, for the Moon. Inferences about planetary
49 cores can be obtained from geodesy, electrical and magnetic data, and size, density, and
50 composition have been estimated (e.g. Yoder et al. 2003; Margot et al. 2007; Rivoldini et al.
51 2009; Zhang and Pommier 2017). However, those inferences require detailed modeling of the
52 interior structure, and the precision of the estimates, in particular core composition, calls for
53 extensive knowledge about core material properties. In this study we investigated the density
54 of liquid Fe-S alloys up to 5 GPa and 1900 K and assessed how it affects the Lunar interior.

55 Simultaneous measurements of density and liquid structure have been performed to
56 emphasize the strong link between evolution of the local atomic arrangement and changes in
57 the liquid density. This experimental study has been complemented by *ab initio* calculations
58 of the liquid structure in similar P-T conditions. We present two models describing
59 thermoelastic properties of liquid Fe-S as a function of pressure, temperature, and S content

60 based on our data and results published in the literature. These models are finally applied to
61 estimate S content in Moon's core.

62

63 **Experimental procedure**

64 *Paris-Edinburgh Press experiments*

65 X-ray diffraction experiments were carried out at the High Pressure beamline ID27 at
66 ESRF in Grenoble, France (Mezouar et al. 2005) using a large volume VX5 type Paris-
67 Edinburgh press (PEP) (Besson et al. 1992; Klotz et al. 2005). This press allows large opening
68 angle in the equatorial plane. The very high brilliance X-ray beam delivered by two in-
69 vacuum undulators was collimated down to 50*50 microns (typical values). The X-ray
70 wavelength was fixed to $\lambda=0.24678$ Å (Gadolinium K-edge) using a Si(111) channel cut
71 monochromator. A multichannel collimator (Mezouar et al. 2002; Morard et al. 2011) was
72 used to minimize the X-ray background coming from sample environment materials. The data
73 were collected using a MAR345 imaging plate system (X-Ray research company GmbH,
74 Nordersted, Germany). The sample-detector distance was calibrated with a LaB₆ standard
75 powder and the diffraction images were treated and integrated using the Fit2D software
76 (Hammersley et al. 1996). Typical exposure time to obtain the hereby presented data is 300s.

77 The high-pressure chamber consists of two opposed tungsten carbide anvils which
78 have quasi-conical hollows. We used 7 mm boron epoxy gaskets with a classical cell
79 assembly (graphite cylinder furnace, MgO capsule used as pressure medium and electrical
80 insulator (Mezouar et al. 1999)). MgO polycrystalline capsule is softer than single crystal
81 alumina capsule, used for conventional X-ray radiography technique, so to minimize pressure
82 gradients in the cell (Nishida et al. 2016). Pressure was calibrated using equation of state
83 (EoS) of MgO (Utsumi et al. 1998) close to the sample, in order to reduce P-T uncertainties.
84 Temperature was fitted using a previously established calibration curve (Morard et al. 2007a).
85 By combined use of this calibration and MgO EoS, pressure was found to be stable up to 1570
86 K and to decrease at higher temperatures (up to 0.7 GPa for the highest temperature). With
87 increasing temperature we could track the structural transitions in Fe (Klotz et al., 2008) and
88 FeS (Urakawa et al., 2004), confirming the validity of the temperature calibration. As
89 addressed in details in a previous paper (Morard et al., 2007b), metrological uncertainties are
90 the following : 170 K in temperature and 0.6 GPa in pressure.

91 The samples were a mixture of pure Fe (99.99 %, Alfa Aesar) and FeS powders
92 (99.9%, Sigma Aldrich). Electron microprobe (EMP) analyses were performed on quenched
93 samples (Centre Camparis, UPMC, Paris) using a Cameca SX100 wavelength dispersive
94 spectrometer (WDS) to measure the three main elements in this study (Fe, S and O, as
95 potential pollutant). Operating conditions in both cases were 15 kV and 40 nA for a counting
96 time of 20 s on peak and 10 s on background. Standards for the three elements were Fe, FeS₂
97 and Fe₂O₃, respectively. Our samples show fine dendritic textures; therefore we used a
98 defocused beam of ~20 microns to average the compositions of quenched texture (**Figure 1**).

99 Density and liquid structure of liquid Fe-S alloys were extracted from the diffuse
100 scattering signal recorded under high pressure and high temperature. Diffuse signal with high
101 quality were recorded on a Q range up to almost 100 nm⁻¹, allowing measurements up to the
102 third oscillation of the structure factor S(Q) (**Figure 2**). Analysis of angle dispersive liquid
103 diffuse signal recorded using PEP is detailed in a previous paper (Morard et al., 2013).
104 Uncertainties on experimentally measured density values of ±3 atoms/nm³ (equivalent to
105 ~250 kg/m³) were estimated from Q range, self-absorption and minimal distance on the radial
106 distribution function g(r) (**Table 1**) (Morard et al, 2013).

107

108 ***Molecular Dynamics Calculations***

109 Simulations were performed using the ABINIT package (Gonze et al. 2016). The
110 electrons are treated quantum mechanically using density functional theory (DFT) while the
111 ions movement is treated classically using the resulting forces. The calculations used the
112 projected augmented wave (PAW) (Blochl 1994; Torrent et al. 2008) method for the
113 computation of the electronic structure and the generalized gradient approximation (GGA)
114 following the parametrization of Perdew, Burke and Ernzerhof (PBE) for the exchange-
115 correlation energy and potential (Perdew et al. 1996). For iron we generated a pseudo-
116 potential with 3s, 3p, 3d, and 4s states as valence electrons (see (Dewaele et al. 2008; Bouchet
117 et al. 2013) for a detailed description of the generation of the pseudopotential and a
118 comparison with recent experimental data). For sulfur the pseudo-potential includes 3s and 3p
119 states as valence electrons. The simulations were performed using a cutoff energy, E_c , for the
120 plane wave basis chosen equal to 350 eV. The radius of the augmentation regions for the
121 PAW pseudo-potential were chosen small enough to avoid an overlapping of the spheres
122 surrounding each atom at the highest densities. An efficient scheme for the parallelization

123 present in ABINIT was used to perform the simulations involving a large number of atoms
124 and time steps (Bottin et al. 2008).

125 We used supercells of liquid Fe of 128 atoms and we replace 13, 17, 29, 38, 50 and 64
126 atoms of Fe by atoms of S to obtain composition of 10%atS, 23%atS, 30%atS, 39%atS, and
127 50%atS respectively. The simulations were first performed in the NPT (constant number of
128 atoms, pressure and temperature) ensemble to reach the desired pressure (5 GPa) and then in
129 the NVT (constant number of atoms, volume and temperature) ensemble in order to avoid any
130 fluctuations of cell parameters. The temperature was fixed to 2500 K and we systematically
131 used an electronic temperature equal to the ionic temperature in our simulations. This
132 relatively high temperature is necessary to ensure the complete melting of the supercells.

133 Once the box of simulated atoms is equilibrated (after at least 5 ps), partial radial
134 distributions functions, $g(r)$, for Fe–Fe, Fe–S and S–S atoms were calculated from 2.5 ps time
135 averages taken different starting times to ensure the convergence. It is well known that at
136 room pressure the experimental equilibrium volume of iron is underestimated in DFT-GGA-
137 PBE calculations due to an incorrect modelling of magnetic effects (Dewaele et al. 2008) by
138 around 7% and therefore the density is overestimated by the same percentage. The bulk
139 modulus is also strongly overestimated (Dewaele et al. 2008), and therefore the density
140 discrepancies between DFT_GGA and experiments hold up to high pressure (around 150
141 GPa). Note that it is possible to correct the GGA results by using the dynamical mean-field
142 theory (Pourovskii et al. 2013) and to recover a good agreement with the experimental
143 equation of state, but this approximation cannot be used in molecular dynamics calculations
144 due to its enormous computational cost. For solid Fe-S in the B2 structure the density
145 overestimation is similar (Sherman 1995). We reproduce these discrepancies in our
146 calculations for liquid Fe-S with a constant overestimation of the experimental density by
147 about 1000 kg/m^3 , due to the GGA-PBE, but also to a larger pressure in the calculations.
148 Noteworthy, the overall evolution of the density as a function of the sulfur composition is
149 comparable to that experimentally measured.

150

151 **Results and discussion**

152 *Liquid structure*

153 Analysis by Fourier transform of the diffuse X-ray scattering of liquid metals gives
154 access to the local structure $g(r)$ of the liquid (Figure 3). In addition to the experimental
155 results, ab initio calculations have been performed on this system in a similar P-T range.
156 As already mentioned, inherent problems of calculations involving iron, without modeling
157 magnetic properties correctly, leads to a known overestimation of the density. However,
158 main features of experimental and theoretical liquid structures are relatively similar. It
159 should be noticed that oscillations present in the experimental data of the structure of pure
160 FeS liquid are not real but are related to spurious signal coming from limited Q range on
161 the corresponding structure factor.

162 Irrespectively of the density shift, simulations bring additional information impossible
163 to obtain with the present XRD experiments: partial $g(r)$ have been be extracted from the
164 calculations (Figure 4), showing no S-S polymerization on the Fe-FeS side of the phase
165 diagram, in agreement with previous published calculations using smaller supercells (64
166 atoms compared to 128 in our MD simulations) (Alfè and Gillan 1998; Vočadlo et al.
167 2000). The S-S bond remains quite large, emphasizing S-S repulsion, and no formation of
168 S-S clusters for all studied compositions. This definitely rules out the idea that S-S
169 interactions were at the origin of the anomalous values of the viscosity (LeBlanc and
170 Secco 1996).

171 Partial $g(r)$ do not show any drastic change in the bond lengths with increasing S
172 content (Figure 4). The Fe-S bond is shorter than the Fe-Fe bond, this is related to the
173 covalent status of this bond (Flory et al. 2005; Morard et al. 2008). The position of the
174 first peak in the $g(r)$, directly related to the first coordinance sphere (CS), was observed in
175 the experiments to remain relatively unchanged up to ~30at%S and to drastically decrease
176 for larger sulfur concentrations (Figure 5). As the contribution of each X-X atomic pair to
177 the total $g(r)$ probed by X-ray is related to the weight of the atoms, the first peak position
178 is essentially associated with the Fe-Fe network. S-S bond is relatively longer (3.4 Å) but
179 with lower intensity and larger dispersion, whereas Fe-S bonds are shorter (2.2 Å) than
180 Fe-Fe bonds (2.5 Å) and have a higher intensity. It is therefore the addition of Fe-S bonds
181 that influence the total $g(r)$ observed in our experiments, and explained the shortening of
182 the observed first CS position (Figure 5). The hereby presented peak position are in
183 relative good agreement with previous results from (Kono et al. 2015).

184

185 *Comparison of our dataset with the literature*

186 The Fe-FeS binary system has been studied extensively over a large pressure range.
187 Density of liquid Fe-S alloys has been determined by ex-situ sink-float method (Balog et al.
188 2003; Nishida et al. 2008), by in situ X-ray radiography (J. Chen et al. 2014), and by X-ray
189 absorption (Sanloup et al. 2000; Nishida et al. 2011). These datasets do not provide a
190 consistent picture, and the derived densities show large discrepancies, even when
191 measurements have been performed with the same method. Sound velocities of liquid Fe-S
192 alloys have been probed in situ under high pressure by conventional ultrasonic method but, as
193 for the density measurements, the results by different research groups are in disagreement
194 (Nishida et al. 2013, 2016; Jing et al. 2014). A thorough comparison of our new
195 measurements (**Table 1**) with literature results will shed light on the properties of the Fe-S
196 binary system at high pressure and high temperature.

197 Regarding pure liquid FeS, previous studies have found contradictory results (Nishida et al.
198 2011; B. Chen et al. 2014) in spite of using the same X-ray absorption technique. Chen et al.
199 argue that the reported density difference can be explained by the temperature difference.
200 Specifically, they claim that temperature difference of 150K can account for a density
201 difference of almost 400 kg/m³. However such a large thermal expansion is incompatible with
202 ambient pressure measurements (for pure FeS, the liquid density only changes from ~3900
203 kg/m³ to ~3820 kg/m³ between 1473 K and 1623 K (Kaiura and Toguri 1979)). Furthermore,
204 a combined fit of either of the two high-pressure sets of density for pure liquid FeS with
205 ambient pressure results is impossible using conventional EoS values, and requires an
206 unrealistically small K_{T0} (Nishida et al. 2011). Conversely, the here-measured density for pure
207 liquid FeS at high pressure are in good agreement with ambient pressure measurements
208 (Nagamori 1969; Kaiura and Toguri 1979), while differ from the previous high-pressure
209 measurements (the difference between the present dataset at 4 GPa and 1900 K and previous
210 determination is 6% (Nishida et al. 2008), 10% (Nishida et al. 2011), and 20 % (J. Chen et al.
211 2014) (**Figure 6**).

212 Unlike liquid density measurements at high pressure, literature concerning measurements
213 on liquid Fe-S alloys at ambient pressure is rather limited and relatively old (Nagamori 1969;
214 Kaiura and Toguri 1979). It should also be noted that there are no density measurements over
215 a wide compositional range (0-40 at% S) at ambient pressure. Regarding pure liquid Fe,
216 measurements have been recently performed over a wide temperature range, allowing a very

217 good estimation of the density/temperature relation (Assael et al. 2006), which is used to
218 extract density of liquid Fe-S alloys at 1900 K as a function of S content (Figure 7).

219 The density of the liquid Fe-S alloys at ambient pressure (ρ_0) is a sensitive parameter in
220 our study. Drastically different models have been used in previous studies (Figure 7), with a
221 deviation of $\sim 1000 \text{ kg/m}^3$ for close compositions in the 15-20 at% S range. We anchor our
222 study on ambient pressure measurements, fixing the density for the 40-50 at% S alloys on
223 those by Nagamori (1969) extrapolated at 1900 K using thermal expansion from Kaiura and
224 Togori (1979). A quadratic polynomial fit is then performed to interpolate between density of
225 S-rich alloys and that of pure liquid Fe, fixed to the value of Assael et al. (2006). This trend is
226 in relative good agreement with densities calculated by ab initio techniques (Kuskov and
227 Belashchenko 2016) for low S concentration (Figure 7). The so-derived second order
228 polynomial gives:

$$229 \quad \rho = -3108X_S^2 - 5176X_S + 6950 \quad (1)$$

230 where X_S is the S concentration in at.%. Looking at this relation, it comes clearly out
231 that values of density from Sanloup et al., (2000) and the related model from Jing et al. (2014)
232 are too low, in particular for low S content, and in disagreement with our model (Figure 7).

233 Regarding sound velocity, most recent measurements (Nishida et al. 2016) and
234 calculations (Kuskov and Belashchenko 2016) are incompatible with ambient pressure
235 measurements (Nasch et al. 1997; Nasch and Manghnani 1998) (Figure 8 and 9), while
236 previous measurements on Fe-16at%S are (Jing et al. 2014) (Figure 9). Our model is therefore
237 adjusted to agree with Jing et al, (2014).

238 To conclude, a survey of the literature on Fe-S liquid alloys under high pressure show
239 relatively scattered results. Strong disagreement exists for density, sound velocity and thermal
240 expansion. Our approach is to anchor our model on ambient pressure measurements, with
241 only few assumptions, as for example the interpolation of liquid density between 0 and 40
242 at% S.

243

244 *Parametrized equation of state*

245 In order to fit our set of density data, we use a 3rd order Birch Murnaghan equation of state
246 relating pressure P and density ρ at the fixed temperature of 1900 K:

247
$$P = \frac{3}{2} K_{T0} \left[\left(\frac{\rho}{\rho_0} \right)^{7/3} - \left(\frac{\rho}{\rho_0} \right)^{5/3} \right] \left[1 + \frac{3}{4} (K'_0 - 4) \left(\left(\frac{\rho}{\rho_0} \right)^{2/3} - 1 \right) \right] \quad (2)$$

248 where K_{T0} is the isothermal bulk modulus at ambient pressure and 1900 K, K' is the
249 pressure derivative of the bulk modulus and ρ_0 is the density at ambient pressure and 1900 K.
250 Each parameter is a function of molar S content in the liquid (X_S). The isothermal bulk
251 modulus at ambient pressure and its derivative can be expressed as follows (J. Chen et al.
252 2014):

253
$$K_{T0} = K_{T,Fe}^{1-X_S} * K_{T,S}^{X_S} \quad (3)$$

254 A linear mixing law for bulk moduli could be used, but for a shorter range of
255 composition (Morard et al. 2013). In the present study, we found more suitable to use such
256 type of mixing law. More details regarding different mixing law for bulk moduli can be found
257 in Chen et al, 2014.

258 For pure Fe we assume $K_{T,Fe}=76$ GPa. This value is deduced from sound velocity
259 measurements at 1bar (Nasch and Manghnani 1998), assuming a value for the specific heat at
260 constant volume C_V of $4R$ and the value of specific heat at constant pressure C_P as in (Nasch
261 and Steinemann 1995). Regarding sulfur, we take $K_{T,S}=1.6$ GPa (Tsuchiya 1994) as in Chen
262 et al. (2014), which gives an overall good agreement with compressibility data from Nishida
263 et al. (2011). However, it should be noticed that this value is measured at 673 K and not at
264 1900 K. Accordingly, this parameter should be rather considered a fitting parameter,
265 restraining the validity of our model only between Fe and FeS compounds.

266 As measurements in the 0-5 GPa range do not cover a large enough pressure range to
267 adequately constrain K' values, this is adjusted to fit the velocity measurements, following the
268 relation $K' = K'_{Fe} + X_S * 3$, with $K'_{Fe} = 6.5$.

269 As our measurements were performed at different temperatures, we also need to
270 estimate thermal expansion as a function of pressure, temperature, and S content. We assume
271 a linear dependence of density on temperature (experimentally proven for liquid iron (Assael
272 et al. 2006)). We calculate the thermal expansion at 1900 K, assuming linearity between Fe
273 and FeS:

274
$$\alpha_0 = -\frac{1}{\rho_0} \left(\frac{\partial \rho}{\partial T} \right)_0 \quad (4)$$

275
$$\left(\frac{\partial \rho}{\partial T} \right)_{Fe,0} = 0.926 \text{ from (Assael et al. 2006)}$$

276
$$\left(\frac{\partial \rho}{\partial T} \right)_{FeS,0} = 0.533 \text{ from (Kaiura and Toguri, 1979)}$$

277
$$\left(\frac{\partial \rho}{\partial T} \right)_0 = \left(\frac{\partial \rho}{\partial T} \right)_{Fe,0} - 2 \left[\left(\frac{\partial \rho}{\partial T} \right)_{Fe,0} - \left(\frac{\partial \rho}{\partial T} \right)_{FeS,0} \right] X_S \quad (5)$$

278 Due to the lack of data on thermal expansion for intermediate compositions, we chose
 279 a linear mixing for the thermal expansion mixing model. More detailed investigation is
 280 required in the future to better constrain this linear model.

281 Then, thermal expansion at a given pressure is calculated under the assumption:

282
$$\alpha_0 K_{T,0} = \alpha K_T \quad (6)$$

283 With

284
$$K_T = \frac{K_{T0}}{2} \left[7 \left(\frac{\rho}{\rho_0} \right)^{7/3} - 5 \left(\frac{\rho}{\rho_0} \right)^{5/3} \right] \left[1 + \frac{3}{4} (K'_0 - 4) \left(\left(\frac{\rho}{\rho_0} \right)^{2/3} - 1 \right) \right] + \frac{3K_{T0}}{4} \left[(K'_0 - 4) \left(\left(\frac{\rho}{\rho_0} \right)^3 - \left(\frac{\rho}{\rho_0} \right)^{7/3} \right) \right]$$

 285
 286 (7)

287 A parameter that could be directly derived from our Eos is the compressional sound
 288 velocity in the liquid:

289
$$V_P = \sqrt{\frac{K_T (1 + \alpha \gamma T)}{\rho}} \quad (8)$$

290 The value of the Grüneisen parameter of the liquid Fe-S alloy is calculated from the
 291 V_P of pure Fe and Fe-16%at. S (Nasch et al. 1997; Nasch and Manghnani 1998) (Figure 8,
 292 inset) assuming that the Grüneisen parameter evolves linearly with the sulfur concentration.
 293 The values obtained are in agreement with ab initio calculations in (Kuskov and
 294 Belashchenko 2016) (Figure 8, inset). However, calculations from (Kuskov and Belashchenko

295 2016) argue for an increase of the sound velocity as a function of S content, whereas
296 experimental data show the opposite behavior (Figure 8). In addition, Grüneisen parameter is
297 assumed to be constant in the pressure range 0-10 GPa. This seems quite reasonable over a
298 relatively small pressure range (Kuskov and Belashchenko 2016). The Grüneisen parameter
299 varies here as $\gamma=1.52+2.5X_S$.

300

301 **Thermodynamic model**

302 In addition to the empirical parametrization introduced above, we also provide a
303 description of the thermoelastic properties of liquid Fe-S alloys based on thermodynamic
304 solution modeling. This approach is complementary to the previous one and is based on the
305 mixing of the end-members: pure liquid Fe and FeS. For liquid Fe we use the EoS of
306 Komabayashi (2014) and for liquid FeS, an EoS deduced from our density data and from
307 sound velocity data of Nishida et al. (2016). For both end-members we use a Vinet equation
308 for isothermal compression and an Anderson-Grüneisen parametrization for isobaric heating
309 (see (Komabayashi 2014). The parameters for liquid FeS EoS are given in Table 2. To assess
310 the solution model that best describes our density data and the sound velocity data of Nishida
311 et al (2016) over the entire Fe-FeS binary, we test three different mixing models that affect the
312 volume of the solution, assuming (a) ideality; (b) concentration dependent non-ideality; and
313 (c) concentration and pressure dependent non-ideality.

314 To model the excess contribution we use the Margules parameterization, introduced by
315 Buono and Walker (2011), to describe the non-ideal behavior of Fe-FeS liquidus on the iron-
316 rich side of the Fe-FeS phase diagram. In this parametrization, the excess contribution to the
317 Gibbs energy is linear in temperature. As a consequence, the thermal expansivity and isobaric
318 heat capacity of the solution depends only on the end-members.

319 The ideal and excess thermoelastic properties of the solution are obtained from its
320 Gibbs energy (e.g. Poirier et al. 2000), and the Grüneisen parameter required for calculating
321 the sound velocity (Eq 8) is computed from

$$322 \quad \gamma = \left(\frac{C_p}{\alpha K_T V} - \alpha T \right)^{-1}, \quad (9)$$

323 where α , K_T , V , and C_p are the thermal expansivity, isothermal bulk-modulus, volume, and isobaric
324 heat capacity of the solution.

325 ***Ideal mixing***

326 The ideal mixing volume between the two end-members is described by the following
327 equation:

$$328 \quad V = (1 - x)V_{Fe} + xV_{FeS}, \quad (10)$$

329 where V is the volume of the considered liquid alloy, x the mole fraction of FeS, and V_{Fe} the
330 volume of liquid Fe and V_{FeS} the volume of liquid FeS.

331 Such a simple model cannot reproduce our density dataset (Figure 10). The density
332 calculated from Eq.10 decreases too rapidly with increasing S concentration and does not
333 reproduce the positive curvature of density as function of S content seen in the data (Figure
334 10).

335 ***Pressure independent volume Margules parameters***

336 In this non-ideal mixing model, the volume is:

$$337 \quad V = (1 - x)V_{Fe} + xV_{FeS} + (1 - x)x(W_{V,Fe} (1 - x) + W_{V,FeS} x), \quad (11)$$

338 where $W_{V,Fe}$ and $W_{V,FeS}$ are the volume Margules parameters. The values of those parameters
339 have been estimated by fitting Eq. 11 on the density data (case A) and on the sound velocity
340 data (case B) separately (Table 3).

341 The density data is well described in case A, but the predicted sound velocities do not
342 agree with the measurements. Conversely, a fit to the sound velocity data provides a good
343 representation for the sound velocity (case B), but fails to describe the experimental density
344 data. This simple Margules mixing model is well suited for modeling the Fe-rich side of the
345 Fe-S phase diagram and the density of Fe-S solutions however, as shown in case B, a different
346 non-ideal behavior is required to describe the sound velocity data. With Eq 11, the sound
347 velocity is only affected by the non-ideality through the volume but not through the bulk
348 modulus. A non-ideal contribution to the bulk modulus requires that the volume Margules
349 coefficients depend on pressure, as discussed in the next section.

350 ***Pressure dependent volume Margules parameters***

351 By trial and error, we have found that the density and sound velocity data can well be
352 described if we adopt the following parametrization for the volume Margules parameters:

353
$$W_{V,Fe} = W_{11} + W_{12} \ln\left(\frac{3}{2} + P\right) \quad (11)$$

354
$$W_{V,FeS} = W_{21} + W_{22} P. \quad (12)$$

355 The estimated values for the parameters W are given in **Table 3**. They have been
356 obtained by fitting the equations describing the volume and sound velocity on the density and
357 sound velocity data at the same time. As can be seen from Fig. 10, this parameterization for
358 the liquid solution gives an adequate description for the experimental data in the 0-8 GPa
359 pressure range. Note that this parametrization cannot be used to model thermoelastic
360 properties beyond that pressure range since an already moderate extrapolation in pressure
361 would lead to unphysical properties.

362

363 **Implications**

364 To infer the size and sulfur content of planetary cores from seismic or geodesy data
365 requires an accurate knowledge of density and velocity properties of solid and liquid iron
366 alloys as a function pressure, temperature and sulfur content. Until now, no consensus on
367 experimental measurements on Fe-S liquid alloys has been reached, with strong
368 contradictions between the different high-pressure studies, and also large disagreement with
369 ambient pressure data. In the present work, we presented new experimental density data of
370 liquid Fe-S alloys at high pressure and high temperature, together with ab initio liquid
371 structure calculations. Combining this new data set and literature data, we were able to
372 establish an empirical and a thermodynamic model for liquid Fe-S solutions that allow to
373 compute thermoelastic properties of the liquid alloy as a function of pressure, temperature,
374 and sulfur concentration.

375 To illustrate the effect of the new density data on the internal structure of small planets,
376 we compare the composition of the Moon's core predicted by our empirical and
377 thermodynamic Fe-S mixing model with a core model assuming ideal mixing between liquid
378 iron and liquid Fe-10wt%S (**Figure 11**). The thermoelastic properties of the core in the ideal
379 mixing model are calculated following (Dumberry and Rivoldini 2015) and are based on the
380 EoS of liquid Fe (Komabayashi 2014) and Fe-10wt%S (Balog et al. 2003). The aim of this
381 model is to emphasize that liquid Fe-S alloys EoS directly affect the Moon's core composition
382 deduced from its radius.

383 For our global Moon model, we use the density profile of the silicate part of the Moon
384 structure deduced by Weber et al. 2011 from seismic data, the core models listed in the
385 previous paragraph, and assume that the entire core is in the liquid state, convecting and
386 composed of iron and sulfur. In order to agree with the most recent moment of inertia estimate
387 (Williams et al. 2014), we had to reduce the density of the upper part of the mantle by about
388 0.1%. The pressure in the planet is calculated by solving the hydrostatic pressure equation and
389 Poisson equation. The temperature profile in the core is obtained by integrating the adiabatic
390 gradient equation in the core (e.g. (Dumberry and Rivoldini 2015)) assuming a core-mantle
391 boundary (CMB) temperature of 1750K. All thermoelastic properties of the core are
392 calculated from the mixing models as a function of pressure, temperature, and composition.

393 Our results show that for a given core radius, models based on the new elastic data require
394 approximately twice the amount of sulfur than models based on an equation of state deduced
395 from previous elastic data (Figure 11). Noteworthy, the sulfur concentrations required by the
396 empirical and the thermodynamic model are very similar, even though when the two models
397 are based on a different sets of acoustic velocity data. Models that agree at 1 sigma with the
398 moment of inertia have a core radius below about 360 km but, the specifics of the core model
399 have only a very negligible effect on the moment inertia of the planet. However, the larger
400 amount of sulfur required by the new elastic data significantly affects the thermal evolution of
401 the core (i.e. the liquidus of the core decreases with increasing S content) and with it the
402 dynamo action, by delaying the onset of crystallization of iron-rich compounds in the core.
403 The present model assumes a specific CMB temperature (1750 K) which is expected in the
404 present day core of the Moon (Laneuville et al. 2014). Lowering the CMB temperature will
405 somewhat increase the sulfur content required for the core to match the mass constraint and
406 initiate the crystallization of iron-rich compounds close to the CMB, since the core isentrope
407 is likely steeper than the liquidus (Williams 2009; Breuer et al. 2015). Irrespectively of the
408 assumptions, the present model is a clear illustration of the impact of our two models on
409 Moon's core composition.

410 The present study, anchored on experimental measurements and theoretical calculations,
411 allows to present a coherent model for planetary cores, with applications ranging from the
412 direct simulations of small planetary cores dynamics to the inversion of seismic data (Garcia
413 et al. 2011; Weber et al. 2011; Antonangeli et al. 2015).

414

415 **Acknowledgements**

416 The authors thank Stany Bauchau (ESRF) for his help with the X-ray experiments.

417 This work was supported by the Planetlab program of the French National Research
418 Agency (ANR), grant No. ANR-12-BS04-001504.

419 A.R. is supported by the Belgian PRODEX program managed by the European Space
420 Agency in collaboration with the Belgian Federal Science Policy Office

421

422

423 **Figure Captions**

424 **Figure 1:** Scanning Electron Microscope (SEM) images of polished cross sections of
425 recovered samples. Here are presented two different compositions, with typical quench
426 textures of S-poor and S-rich liquids. Microprobe measurements were performed on large
427 area, of ~20 microns, in order to average the composition over these textures.

428

429 **Figure 2:** Structure factors $S(Q)$ of liquid Fe-S alloys as a function of the composition for
430 similar P-T conditions.

431

432 **Figure 3:** Comparison between pair distribution function $g(r)$ obtained from ab initio
433 calculations (5 GPa and 2500 K) and experimental results (similar P-T conditions and
434 composition as in [Figure 2](#)).

435

436 **Figure 4:** Partial pair distribution function for different composition extracted from the ab
437 initio calculations.

438

439 **Figure 5:** First peak position as a function of the S content for the different $g(r)$, compared
440 with theoretical work, and previous results from (Kono et al. 2015).

441

442 **Figure 6:** Density of liquid iron alloys from this study and the corresponding thermodynamic
443 model compared with available measurements. The color of the different symbol is related to
444 the composition, rounded to the closest nominal value.

445

446 **Figure 7:** Density of liquid Fe-S alloys at ambient pressure from different studies. Our
447 thermodynamic model uses an interpolation between the density of pure Fe from (Assael et al.
448 2006) and densities of S-rich liquids (Nagamori 1969) corrected for temperature difference
449 following (Kaiura and Toguri 1979).

450

451 **Figure 8:** Sound velocity fit for this model as a function of S content based on measurements
452 at ambient pressure from (Nasch et al. 1997; Nasch and Manghnani 1998), compared with
453 theoretical calculations from Kuskov and Belashchenko (2016). Inset: Gruneisen parameter
454 used in this model compared with ab initio calculations from Kuskov and Belashchenko
455 (2016).

456

457 **Figure 9:** Sound velocity extracted from our thermodynamic model compared to the available
458 literature (Nasch et al. 1997; Nasch and Manghnani 1998; Jing et al. 2014; Nishida et al.
459 2016). Different colors correspond to different compositions, rounded to the closest nominal
460 value. Representative error bars for the two high pressure studies have been added in the
461 figure legend.

462

463 **Figure 10:** Thermodynamic models of density and sound velocity of liquid Fe-S alloys at
464 1900 K. Four different models have been tested: ideal solution, pressure independent (Model
465 A and B) and pressure dependent Margules parameters. It is clear that the pressure
466 dependence of the Margules parameters is required to represent adequately the experimental
467 values.

468

469 **Figure 11:** Radius of Moon's core as a function of S content of an entirely liquid core, using
 470 models presented in this study (parametrized EoS and thermodynamic model) compared with
 471 an ideal solution based on previous density measurements (Balog et al. 2003). Calculations
 472 were performed for a temperature at the Moon CMB of 1750 K.

473

474 **Tables**

Run number	Pressure (GPa)	Temperature (K)	xS (at%)	density (atoms/nm ³)	Density (kg/m ³)	Density at 1900 K		r1	
						(kg/m ³)	CN1	CN2	(nm)
31-32	4,2 ± 0,6	1900 ± 170	9.9	76,9 ± 3	6830 ± 270	6830 ± 270	8,05	9,26	2,564
34-35	4,1 ± 0,6	1980 ± 170	9.9	76,1 ± 3	6760 ± 270	6840 ± 270	7,94	9,12	2,567
61-62	2,2 ± 0,6	1780 ± 170	9.9	75,8 ± 3	6730 ± 270	6630 ± 270	7,97	9,18	2,578
65-66	2,1 ± 0,6	1860 ± 170	9.9	75 ± 3	6660 ± 270	6630 ± 270	7,85	9,05	2,581
35-36	3,2 ± 0,6	1860 ± 170	17.4	76,4 ± 3	6560 ± 260	6520 ± 260	7,88	9,14	2,569
49-50	2,9 ± 0,6	1780 ± 170	22.9	74 ± 3	6190 ± 250	6090 ± 250	7,64	8,88	2,571
53-54	2,9 ± 0,6	1860 ± 170	22.9	73,4 ± 3	6140 ± 250	6110 ± 250	7,54	8,75	2,572
89-90	1,7 ± 0,6	1780 ± 170	22.9	70,4 ± 3	5890 ± 250	5790 ± 250	7,32	8,45	2,59
91-92	1,5 ± 0,6	1860 ± 170	22.9	70 ± 3	5860 ± 250	5830 ± 250	7,26	8,4	2,589
42	5 ± 0,6	1750 ± 170	29.4	75,2 ± 3	6100 ± 240	5980 ± 240	7,71	8,95	2,552
63	2,7 ± 0,6	1690 ± 170	29.4	72,2 ± 3	5860 ± 240	5690 ± 240	7,43	8,61	2,566
17	3,5 ± 0,6	1600 ± 170	38	71,9 ± 3	5590 ± 230	5370 ± 230	6,86	8	2,543
25	5,2 ± 0,6	1870 ± 170	50	59,8 ± 3	4360 ± 220	4340 ± 220	3,96	4,5	2,415
48	2,6 ± 0,6	1770 ± 170	50	57,3 ± 3	4180 ± 220	4100 ± 220	3,77	4,28	2,423

475

476 **Table 1:** Pressure-temperature conditions, chemical composition of quenched samples,
 477 densities measured and calculated at 1900 K.

478

Reference temperature T0 (K)	1650
Reference volume (after Nagamori corrected for T=1650 K) (cm ³ /mol)	11.8
Reference thermal expansion (after Kaiura) (K ⁻¹)	1.29E-04
KT0 (Gpa)	16.5 (0.5)
K'T0	6.21
γ	1
Q	0

479

480 **Table 2:** Parameters for liquid FeS Equation of state, following Vinet and Anderson-
 481 Gruneisen parameterization (see (Komabayashi 2014) more details).

Model A Model B

$W_{V,Fe}$	-6.74 ± 0.63	4.93 ± 0.92
$W_{V,FeS}$	-0.47 ± 0.51	5.70 ± 0.87
	P dependent model	
W11	-7.78 ± 0.95	
W12	2.31 ± 0.14	
W21	-2.32 ± 0.88	
W22	0.057 ± 0.024	

482

483

484 **Table 3:** Margules parameters for pressure independent and pressure dependent
485 parameterization. These parameters are given cm^3/mol .

486

487 **Bibliography**

488

489 Alfè, , and Gillan, M.J. (1998) First-principles simulations of liquid Fe-S under Earth ' s
490 core conditions. *Physical Review B*, 58, 8248–8256.

491 Andrault, D., Bolfan-Casanova, N., Ohtaka, O., Fukui, H., Arima, H., Fialin, M., and
492 Funakoshi, K. (2009) Melting diagrams of Fe-rich alloys determined from synchrotron in
493 situ measurements in the 15-23 GPa pressure range. *Physics of the Earth and Planetary*
494 *Interiors*, 174, 181–191.

495 Antonangeli, D., Morard, G., Schmerr, N.C., Komabayashi, T., Krisch, M., Fiquet, G., Fei,
496 Y., and Mao, H.-K. (2015) Toward a mineral physics reference model for the Moon's
497 core. *Proceedings of the National Academy of Sciences of the United States of America*,
498 112.

499 Assael, M.J., Kakosimos, K., Banish, R.M., Brillo, J., Egry, I., Brooks, R., Queded, P.N.,
500 Mills, K.C., Nagashima, A., Sato, Y., and others (2006) Reference Data for the Density
501 and Viscosity of Liquid Aluminum and Liquid Iron. *Journal of Physical and Chemical*
502 *Reference Data*, 35, 285–300.

503 Balog, P.S., Secco, R.A., Rubie, D.C., and Frost, D.J. (2003) Equation of state of liquid Fe-10
504 wt % S: Implications for the metallic cores of planetary bodies. *Journal Of Geophysical*
505 *Research-Solid Earth*, 108.

506 Besson, J.M., Nelmes, R.J., Hamel, G., Loveday, J.S., Weill, G., and Hull, S. (1992) Neutron
507 diffraction above 10 GPa. *Physica B: Condensed Matter*, 181, 907–910.

508 Blochl, P.E. (1994) Projector augmented-wave method. *Physical Review B*, 50.

509 Bottin, F., Leroux, S., Knyazev, A., and Zérah, G. (2008) Large-scale ab initio calculations
510 based on three levels of parallelization. *Computational Materials Science*, 42, 329–336.

511 Bouchet, J., Mazevet, S., Morard, G., Guyot, F., and Musella, R. (2013) Ab initio equation of
512 state of iron up to 1500 GPa. *Physical Review B - Condensed Matter and Materials*
513 *Physics*, 87, 1–8.

514 Breuer, D., Rueckriemen, T., and Spohn, T. (2015) Iron snow, crystal floats, and inner-core
515 growth: modes of core solidification and implications for dynamos in terrestrial planets

- 516 and moons. *Progress in Earth and Planetary Science*, 2, 1–26.
- 517 Buono, A.S., and Walker, D. (2011) The Fe-rich liquidus in the Fe-FeS system from 1bar to
518 10GPa. *Geochimica et Cosmochimica Acta*, 75, 2072–2087.
- 519 Campbell, A.J., Seagle, C.T., Heinz, D.L., Shen, G., and Prakapenka, V.B. (2007) Partial
520 melting in the iron-sulfur system at high pressure: A synchrotron X-ray diffraction study.
521 *Physics of the Earth and Planetary Interiors*, 162, 119–128.
- 522 Chabot, N.L. (2004) Sulfur contents of the parental metallic cores of magmatic iron
523 meteorites. *Geochimica Cosmochimica Acta*, 68, 3607–3618.
- 524 Chen, B., Gao, L., Leinenweber, K., Wang, Y., Sanehira, T., and Li, J. (2008a) In situ
525 investigation of high-pressure melting behavior in the Fe-S system using synchrotron X-
526 ray radiography. *High Pressure Research*, 28, 315–326.
- 527 Chen, B., Li, J., and Hauck, S.A. (2008b) Non-ideal liquidus curve in the Fe-S system and
528 Mercury’s snowing core. *Geophysical Research Letters*, 35, 10–14.
- 529 Chen, B., Li, Z., Zhang, D., Liu, J., Hu, M.Y., Zhao, J., Bi, W., Alp, E.E., Xiao, Y., Chow, P.,
530 and others (2014) Hidden carbon in Earth’s inner core revealed by shear softening in
531 dense Fe₇C₃. *Proceedings of the National Academy of Sciences*, 111, 17755–17758.
- 532 Chen, J., Yu, T., Huang, S., Girard, J., and Liu, X. (2014) Compressibility of liquid FeS
533 measured using X-ray radiograph imaging. *Physics of the Earth and Planetary Interiors*,
534 228, 294–299.
- 535 Chudinovskikh, L., and Boehler, R. (2007) Eutectic melting in the system Fe-S to 44??GPa.
536 *Earth and Planetary Science Letters*, 257, 97–103.
- 537 Dewaele, A., Torrent, M., Loubeyre, P., and Mezouar, M. (2008) Compression curves of
538 transition metals in the Mbar range: Experiments and projector augmented-wave
539 calculations. *Physical Review B - Condensed Matter and Materials Physics*, 78, 1–13.
- 540 Dumberry, M., and Rivoldini, A. (2015) Mercury ’ s inner core size and core-crystallization
541 regime. *ICARUS*, 248, 254–268.
- 542 Flory, M.A., McLamarrah, S.K., and Ziurys, L.M. (2005) High-resolution spectroscopy of
543 CoS (X 4 ?? i): Examining 3d transition-metal sulfide bonds. *Journal of Chemical*
544 *Physics*, 123, 1–9.
- 545 Garcia, R.F., Gagnepain-beyneix, J., Chevrot, S., and Lognonné, P. (2011) Very preliminary
546 reference Moon model. *Physics of the Earth and Planetary Interiors*, 188, 96–113.
- 547 Gonze, X., Jollet, F., Abreu Araujo, F., Adams, D., Amadon, B., Applencourt, T., Audouze,
548 C., Beuken, J.M., Bieder, J., Bokhanchuk, A., and others (2016) Recent developments in
549 the ABINIT software package. *Computer Physics Communications*, 205, 106–131.
- 550 Greenwood, R.C., Franchi, I.A., Jambon, A., Barrat, J.A., and Burbine, T.H. (2006) Oxygen
551 Isotope Variation in Stony-Iron Meteorites. *Science*, 313, 1763.
- 552 Hammersley, A.P., Svensson, S.O., Hanfland, M., Fitch, A.N., and Hausermann, D. (1996)
553 Two-dimensionnal detector software: from real detector to idealised image or two-theta
554 scan. *High Pressure Research*, 14, 235–248.
- 555 Jing, Z., Wang, Y., Kono, Y., Yu, T., Sakamaki, T., Park, C., Rivers, M.L., Sutton, S.R., and
556 Shen, G. (2014) Sound velocity of Fe-S liquids at high pressure: Implications for the
557 Moon’s molten outer core. *Earth and Planetary Science Letters*, 396, 78–87.

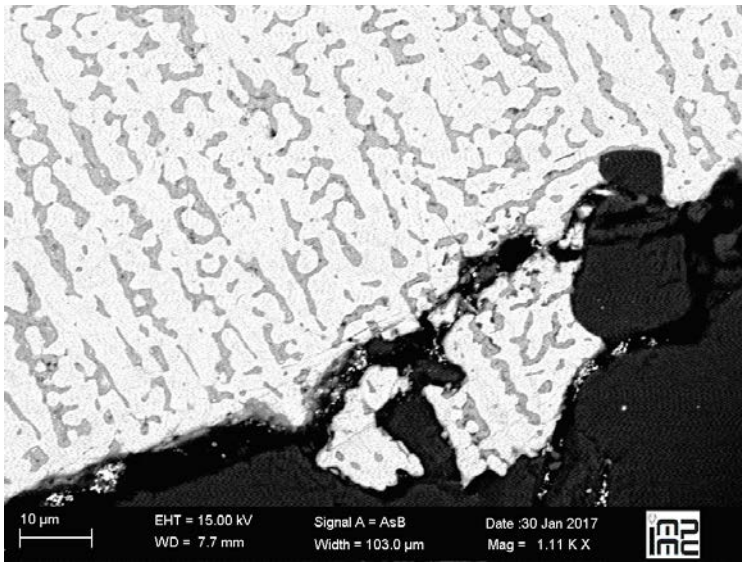
- 558 Kaiura, G.H., and Toguri, J.M. (1979) Densities of the molten FeS, FeS–Cu₂S and Fe–S–O
559 systems—utilizing a bottom-balance Archimedean technique. Canadian Metallurgical
560 Quarterly, 18, 155–164.
- 561 Kamada, S., Ohtani, E., Terasaki, H., Sakai, T., Miyahara, M., Ohishi, Y., and Hirao, N.
562 (2012) Melting relationships in the Fe–Fe₃S system up to the outer core conditions. Earth
563 and Planetary Science Letters, 359–360, 26–33.
- 564 Kleine, T., Touboul, M., Bourdon, B., Nimmo, F., Mezger, K., Palme, H., Jacobsen, S.B.,
565 Yin, Q., and Halliday, A.N. (2009) Hf–W chronology of the accretion and early
566 evolution of asteroids and terrestrial planets. Geochimica et Cosmochimica Acta, 73,
567 5150–5188.
- 568 Klotz, S., Strässle, T., Rouse, G., Hamel, G., and Pomjakushin, V. (2005) Angle-dispersive
569 neutron diffraction under high pressure to 10 GPa. Applied Physics Letters, 86, 1–3.
- 570 Komabayashi, T. (2014) Thermodynamics of melting relations in the system Fe–FeO at high
571 pressure: Implications for oxygen in the Earth’s core. Journal of Geophysical Research :
572 Solid Earth, 119, 4164–4177.
- 573 Kono, Y., Kenney-Benson, C., Shibasaki, Y., Park, C., Shen, G., and Wang, Y. (2015) High-
574 pressure viscosity of liquid Fe and FeS revisited by falling sphere viscometry using
575 ultrafast X-ray imaging. Physics of the Earth and Planetary Interiors, 241, 57–64.
- 576 Kuskov, O.L., and Belashchenko, D.K. (2016) Thermodynamic properties of Fe–S alloys from
577 molecular dynamics modeling: Implications for the lunar fluid core. Physics of the Earth
578 and Planetary Interiors, 258, 43–50.
- 579 Laneuville, M., Wiczorek, M.A., Breuer, D., Aubert, J., Morard, G., and Rückriemen, T.
580 (2014) A long-lived lunar dynamo powered by core crystallization. Earth and Planetary
581 Science Letters, 401.
- 582 LeBlanc, G.E., and Secco, R.A. (1996) Viscosity of an Fe–S liquid up to 1300 degrees C and
583 5 GPa. Geophysical Research Letters, 23, 213–216.
- 584 Margot, J.L., Peale, S.J., Jurgens, R.F., Slade, M.A., and Holin, I. V (2007) Large Longitude
585 Libration of Mercury Reveals a Molten Core. Science, 316, 710–714.
- 586 Mezouar, M., Le Bihan, T., Libotte, H., Le Godec, Y., and Häusermann, D. (1999) Paris-
587 Edinburgh large-volume cell coupled with a fast imaging plate system for structural
588 investigation at high pressure and high-temperature. Journal of Synchrotron Radiation, 6,
589 1115–1119.
- 590 Mezouar, M., Faure, P., Crichton, W., Rambert, N., Sitaud, B., Bauchau, S., and Blattmann,
591 G. (2002) Multichannel collimator for structural investigation of liquids and amorphous
592 materials at high pressures and temperatures. Review of Scientific Instruments, 73, 3570.
- 593 Mezouar, M., Crichton, W.A., Bauchau, S., Thurel, F., Witsch, H., Torrecillas, F., Blattman,
594 G., Marion, P., Dabin, Y., Chavanne, J., and others (2005) Development of a new state-
595 of-the-art beamline optimized for monochromatic single crystal and powder X-ray
596 diffraction under extreme conditions at the ESRF. Journal of Synchrotron Radiation, 12,
597 659–664.
- 598 Morard, G., Mezouar, M., Rey, N., Poloni, R., Merlen, A., Le Floch, S., Toulemonde, P.,
599 Pascarelli, S., San-Miguel, A., Sanloup, C., and others (2007a) Optimization of Paris-
600 Edinburgh press cell assemblies for in situ monochromatic X-ray diffraction and X-ray
601 absorption. High Pressure Research, 27.

- 602 Morard, G., Sanloup, C., Fiquet, G., Mezouar, M., Rey, N., Poloni, R., and Beck, P. (2007b)
603 Structure of eutectic Fe-FeS melts to pressures up to 17 GPa: Implications for planetary
604 cores. *Earth and Planetary Science Letters*, 263, 128–139.
- 605 Morard, G., Andrault, D., Guignot, N., Sanloup, C., Mezouar, M., Petitgirard, S., and Fiquet,
606 G. (2008) In situ determination of Fe-Fe₃S phase diagram and liquid structural properties
607 up to 65 GPa. *Earth and Planetary Science Letters*, 272, 620–626.
- 608 Morard, G., Sanloup, C., Guillot, B., Fiquet, G., Mezouar, M., Perrillat, J.P., Garbarino, G.,
609 Mibe, K., Komabayashi, T., and Funakoshi, K. (2008) In situ structural investigation of
610 Fe-S-Si immiscible liquid system and evolution of Fe-S bond properties with pressure.
611 *Journal of Geophysical Research: Solid Earth*, 113, 1–12.
- 612 Morard, G., Mezouar, M., Bauchau, S., Alvarez-Murga, M., Hodeau, J.L., and Garbarino, G.
613 (2011) High efficiency multichannel collimator for structural studies of liquids and low-
614 Z materials at high pressures and temperatures. *Review of Scientific Instruments*, 82, 2–
615 7.
- 616 Morard, G., Siebert, J., Andrault, D., Guignot, N., Garbarino, G., Guyot, F., and Antonangeli,
617 D. (2013) The Earth's core composition from high pressure density measurements of
618 liquid iron alloys. *Earth and Planetary Science Letters*, 373.
- 619 Nagamori, M. (1969) Density of molten Ag–S, Cu–S, Fe–S, and Ni–S systems. *Transactions*
620 *of the Metallurgical Society AIME*, 245, 1897–1902.
- 621 Nasch, P., Manghnani, M., and Secco, R. (1997) Anomalous behavior of sound velocity and
622 attenuation in liquid Fe-Ni-S. *Science*, 277, 219.
- 623 Nasch, P.M., and Manghnani, M.H. (1998) Molar Volume , Thermal Expansion , and Bulk
624 Modulus in Liquid Fe-Ni Alloys at 1 Bar : Evidence for Magnetic Anomalies ?
625 *Geophysical Monograph*, 101, 307–317.
- 626 Nasch, P.M., and Steinemann, S.G. (1995) Density and Thermal Expansion of Molten
627 Manganese , Iron , Nickel , Copper , Aluminum and Tin by Means of the Gamma-Ray
628 Attenuation Technique GAMMA-RAY ATTENUATION TECHNIQUE. *Physics and*
629 *Chemistry of Liquids*, 29, 43–58.
- 630 Nishida, K., Terasaki, H., Ohtani, E., and Suzuki, A. (2008) The effect of sulfur content on
631 density of the liquid Fe-S at high pressure. *Physics and Chemistry of Minerals*, 35, 417–
632 423.
- 633 Nishida, K., Ohtani, E., Urakawa, S., Suzuki, A., Sakamaki, T., Terasaki, H., and Katayama,
634 Y. (2011) Density measurements of liquid FeS at high pressures using synchrotron X-ray
635 absorption. *American Mineralogist*, 96, 864–868.
- 636 Nishida, K., Kono, Y., Terasaki, H., Takahashi, S., Ishii, M., Shimoyama, Y., Higo, Y.,
637 Funakoshi, K.I., Irifune, T., and Ohtani, E. (2013) Sound velocity measurements in
638 liquid Fe-S at high pressure: Implications for Earth's and lunar cores. *Earth and*
639 *Planetary Science Letters*, 362, 182–186.
- 640 Nishida, K., Suzuki, A., Terasaki, H., Shibasaki, Y., Higo, Y., Kuwabara, S., Shimoyama, Y.,
641 Sakurai, M., Ushioda, M., Takahashi, E., and others (2016) Towards a consensus on the
642 pressure and composition dependence of sound velocity in the liquid Fe-Fe₃S system.
643 *Physics of the Earth and Planetary Interiors*, 257, 230–239.
- 644 Perdew, J.P., Burke, K., and Ernzerhof, M. (1996) Generalized gradient approximation made
645 simple. *Physical Review Letters*, 77, 3865–3868.

- 646 Poirier, J.P. (1994) Light elements in the Earth's outer core: A critical review. *Physics of the*
647 *Earth and Planetary Interiors*, 85, 319–337.
- 648 Pourovskii, L. V., Miyake, T., Simak, S.I., Ruban, A. V., Dubrovinsky, L., and Abrikosov,
649 I.A. (2013) Electronic properties and magnetism of iron at the Earth's inner core
650 conditions. *Physical Review B - Condensed Matter and Materials Physics*, 87.
- 651 Rivoldini, A., Van Hoolst, T., and Verhoeven, O. (2009) The interior structure of Mercury
652 and its core sulfur content. *Icarus*, 201, 12–30.
- 653 Sanloup, C., Guyot, F., Gillet, P., Fiquet, G., Mezouar, M., and Martinez, I. (2000) Density
654 measurements of liquid Fe-S alloys at high pressure. *Geophysical Research Letters*, 27,
655 811–814.
- 656 Sherman, D.M. (1995) pressure and the composition of the Earth ' s core. *Earth and Planetary*
657 *Science Letters*, 132, 87–98.
- 658 Stewart, A.J., Schmidt, M.W., van Westrenen, W., and Liebske, C. (2007) Mars: A New
659 Core-Crystallization Regime. *Science*, 316, 1323–1325.
- 660 Torrent, M., Jollet, F., Bottin, F., Zérah, G., and Gonze, X. (2008) Implementation of the
661 projector augmented-wave method in the ABINIT code: Application to the study of iron
662 under pressure. *Computational Materials Science*, 42, 337–351.
- 663 Tsuchiya, Y. (1994) The thermodynamics of structural changes in the liquid sulphur-tellurium
664 system: compressibility and Ehrenfest's relations. *Journal of Physics: Condensed Matter*,
665 6, 2451.
- 666 Utsumi, W., Weidner, D.J., and Liebermann, R.C. (1998) Volume measurement of MgO at
667 high pressures and high temperatures. *Geophysical Monograph*, 101, 327–333.
- 668 Vočadlo, L., Alfè, D., rice, G.D., and Gillan, M.J. (2000) First principles calculations on the
669 diffusivity and viscosity of liquid Fe-S at experimentally accessible conditions. *Physics*
670 *of the Earth and Planetary Interiors*, 120, 145–152.
- 671 Weber, R.C., Lin, P.-Y., Garnero, E.J., Williams, Q., and Lognonne, P. (2011) Seismic
672 Detection of the Lunar Core. *Science*, 331, 309–312.
- 673 Williams, J.G., Konopliv, A.S., Boggs, D.H., Park, R.S., Yuan, D., Lemoine, F.G., Goossens,
674 S., Mazarico, E., Nimmo, F., Weber, R.C., and others (2014) Lunar interior properties
675 from the GRAIL mission. *Journal of Geophysical Research : Planets*, 119, 1546–1578.
- 676 Williams, Q. (2009) Bottom-up versus top-down solidification of the cores of small solar
677 system bodies: Constraints on paradoxical cores. *Earth and Planetary Science Letters*,
678 284, 564–569.
- 679 Yoder, C.F., Konopliv, A.S., Yuan, D.N., Standish, E.M., and Folkner, W.M. (2003) Fluid
680 Core Size of Mars from Detection of the Solar Tide. *Science*, 300, 299–303.
- 681 Yoshino, T., Walter, M.J., and Katsura, T. (2003) Core formation in planetesimals triggered
682 by permeable flow. *Nature*, 422, 154–157.
- 683 Zhang, Z., and Pommier, A. (2017) Electrical Investigation of Metal-Olivine Systems and
684 Application to the Deep Interior of Mercury. *Journal of Geophysical Research: Planets*,
685 122, 2702–2718.
- 686

Figure 1

Fe + 9.9 at%S



Fe + 38 at%S

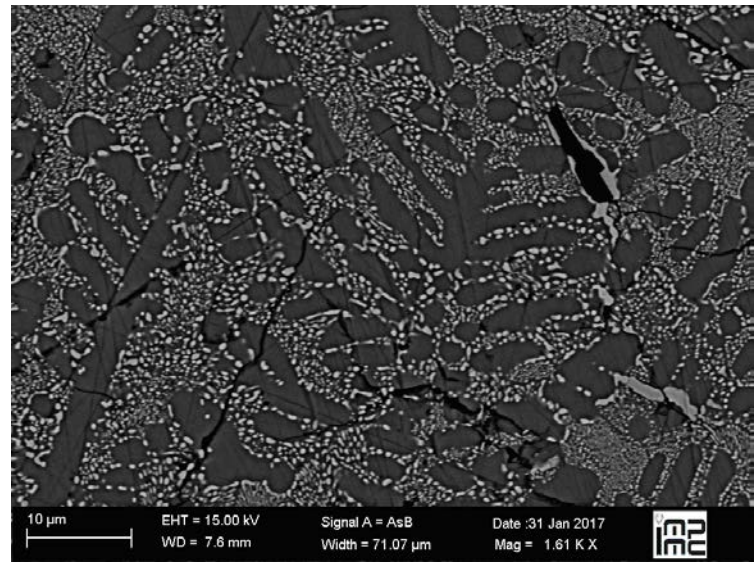


Figure 2

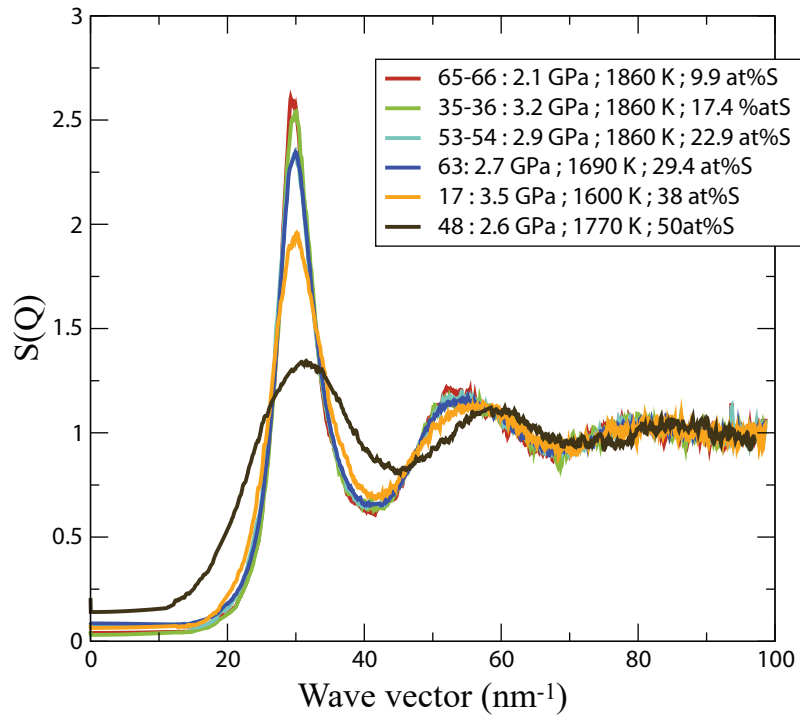


Figure 3

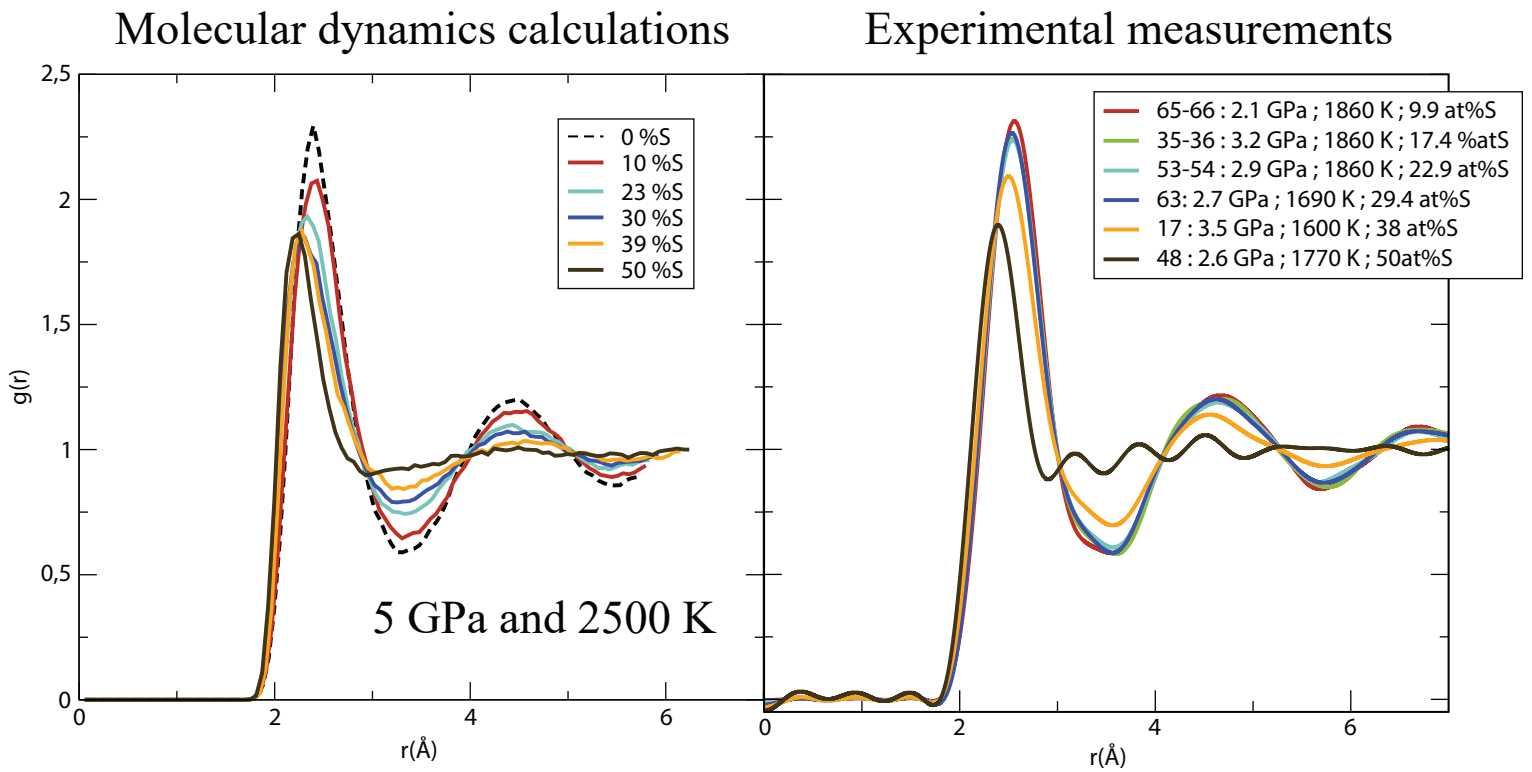


Figure 4

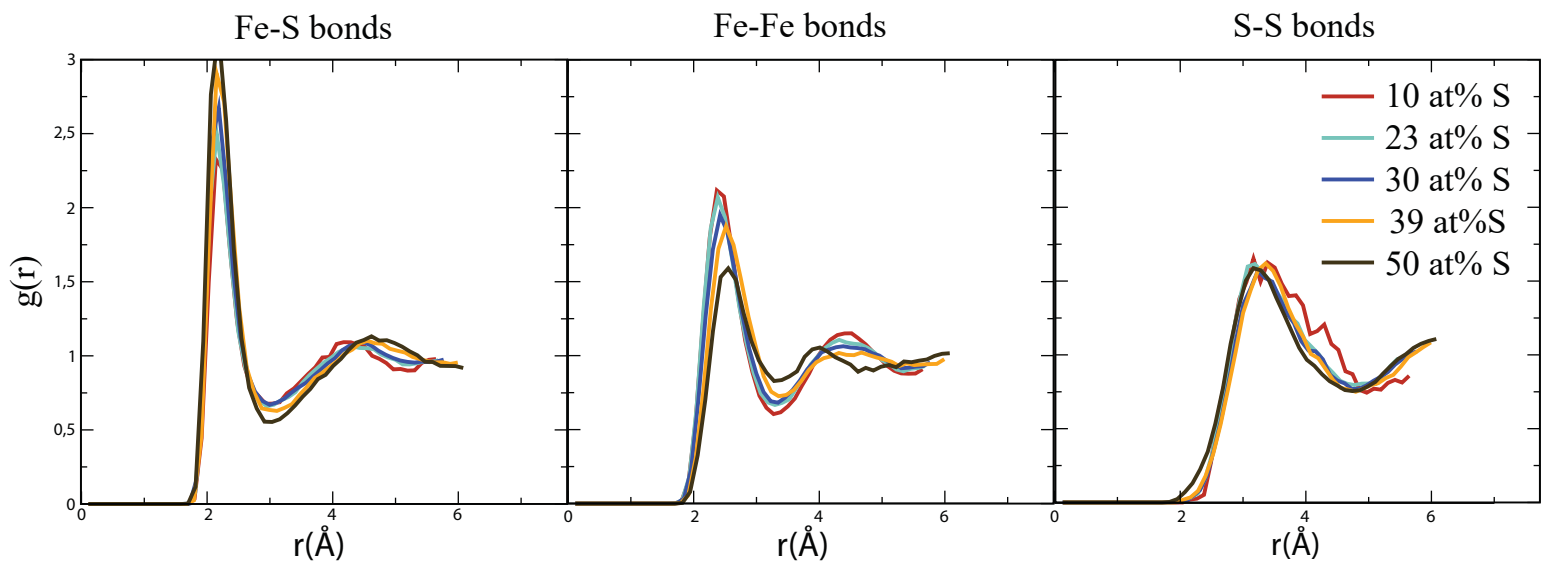


Figure 5

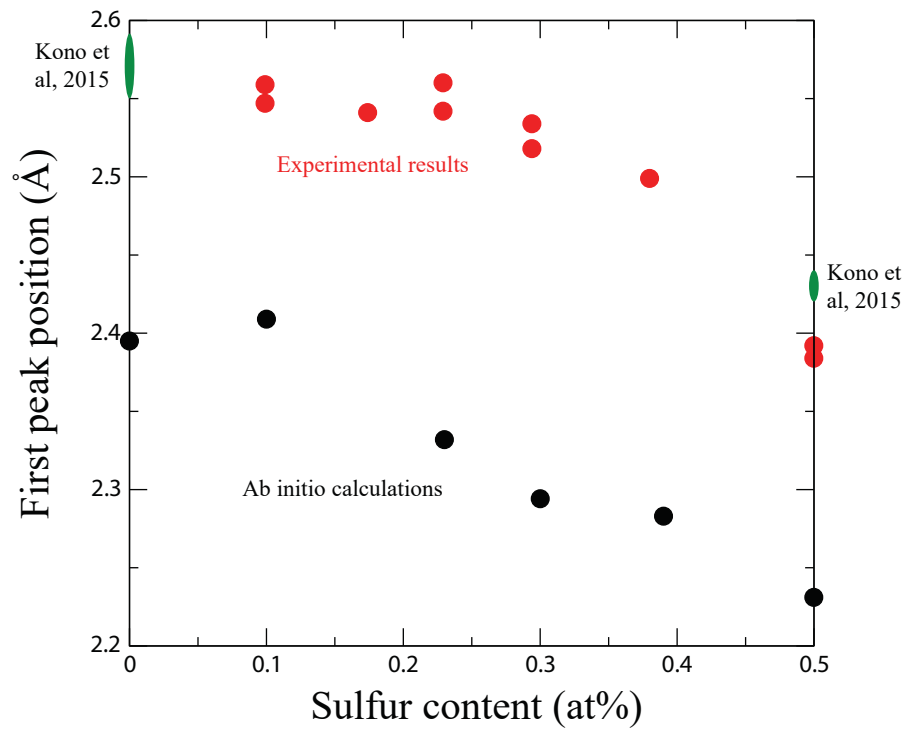


Figure 6

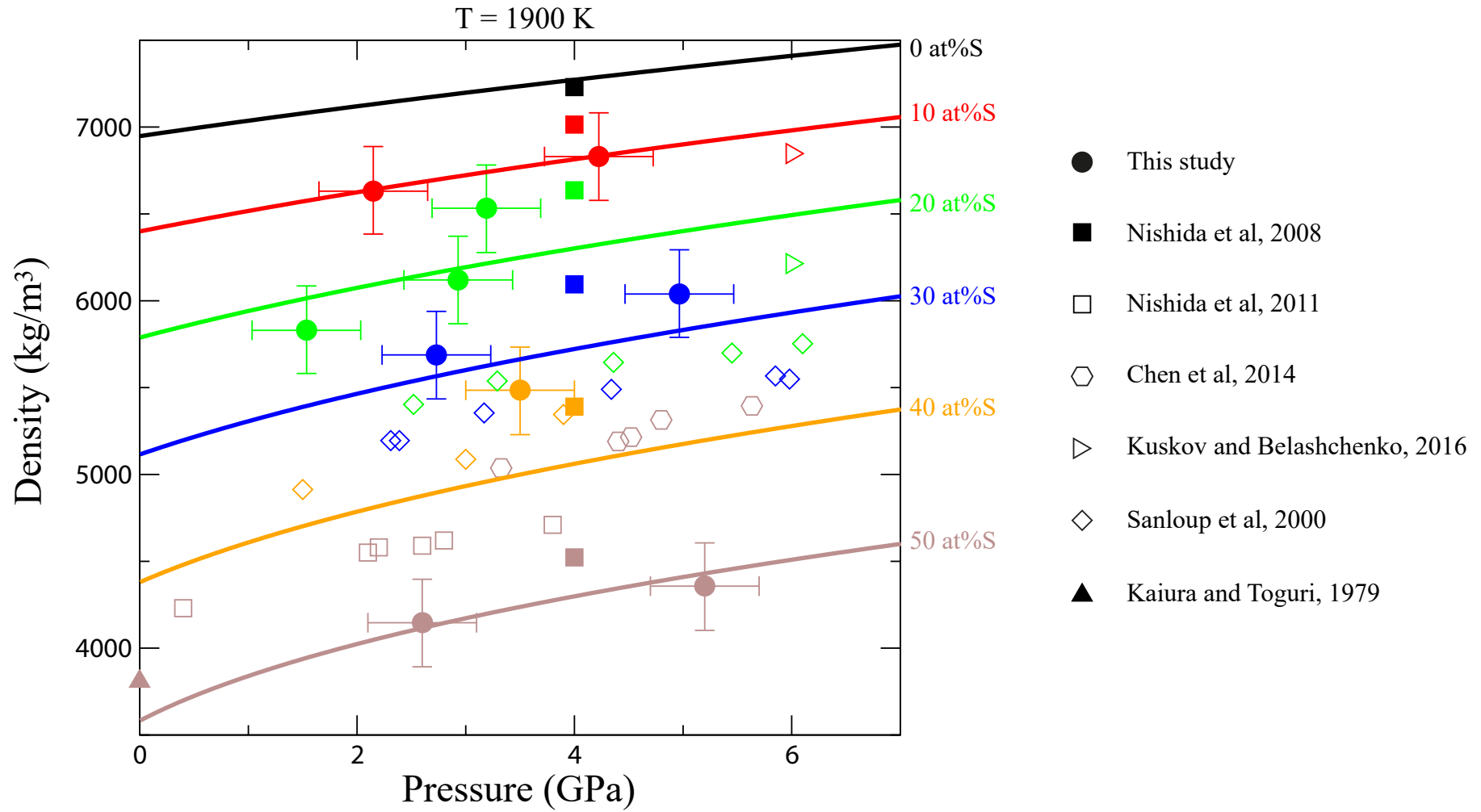


Figure 7

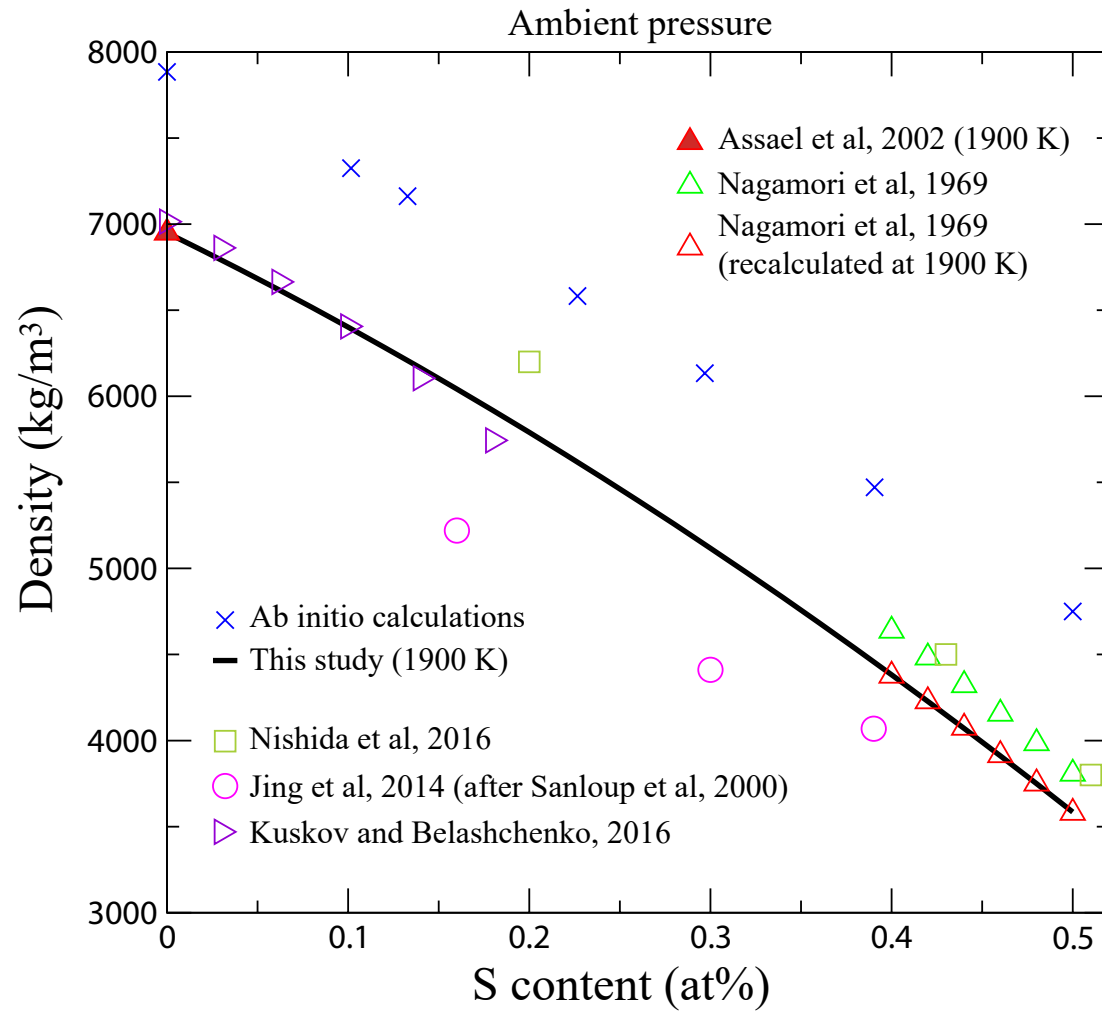


Figure 8

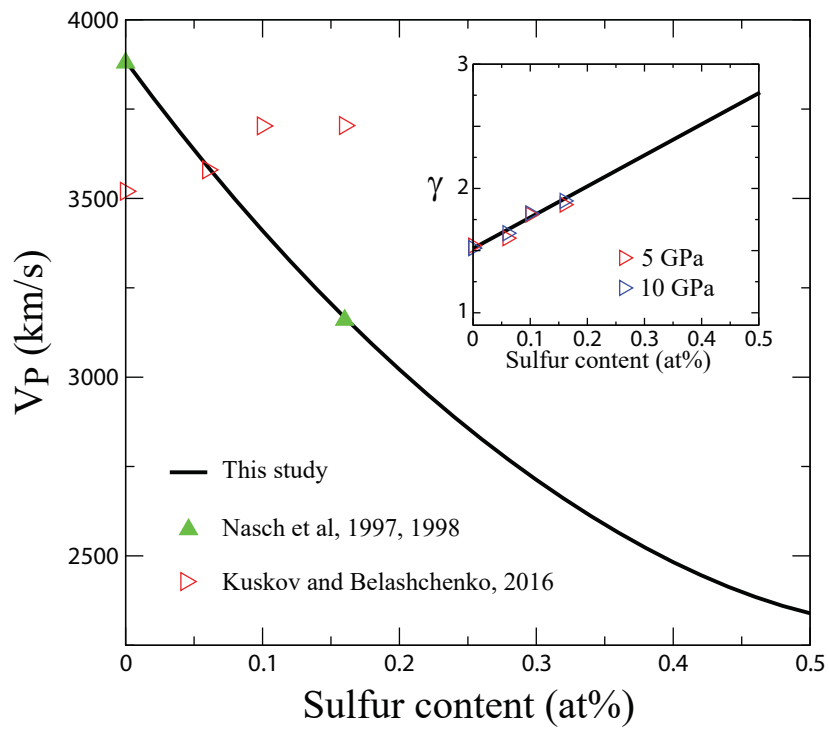


Figure 9

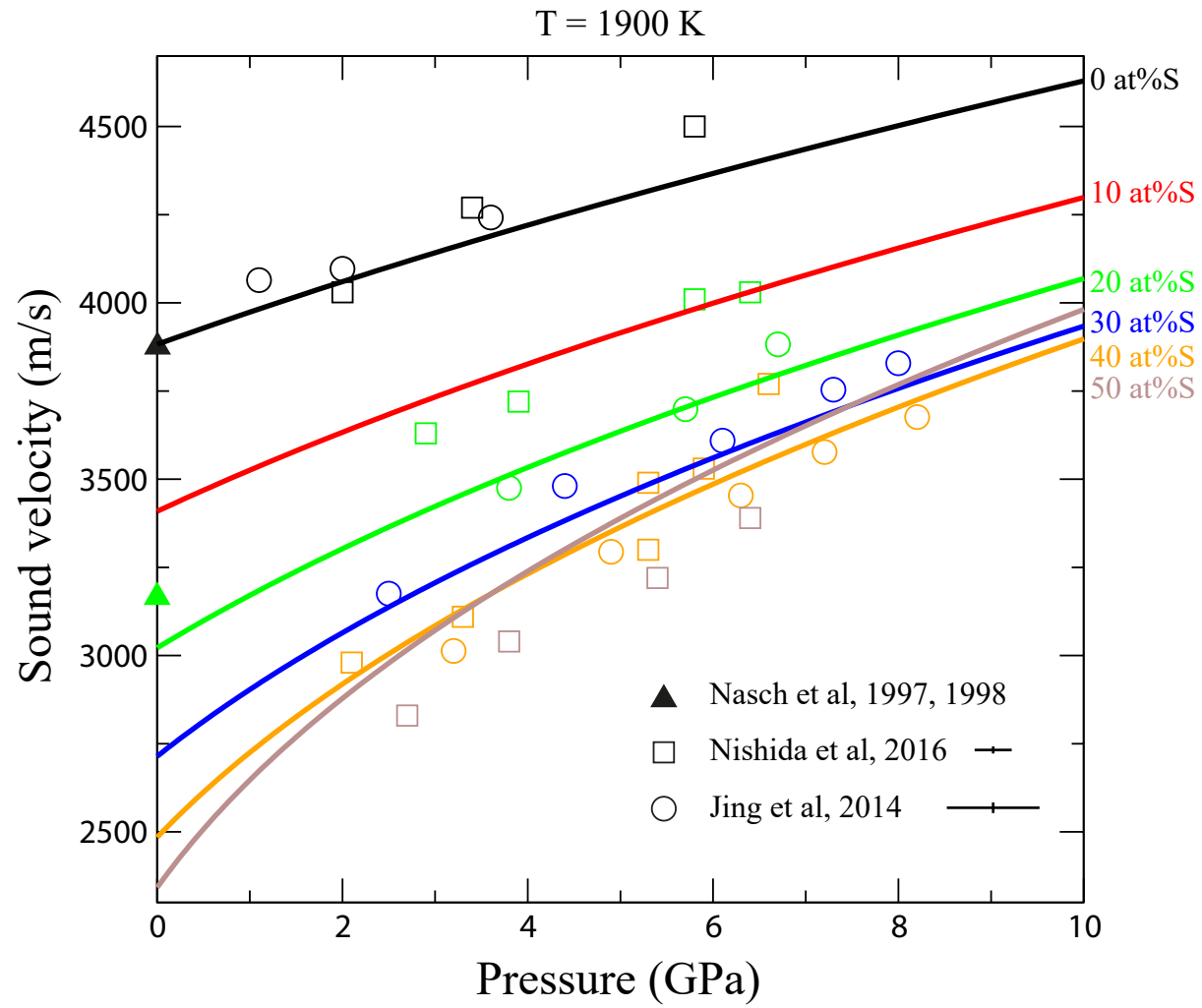


Figure 10

Ideal solution

Pressure independent
Margules model A

Pressure independent
Margules model B

Pressure dependent
Margules model

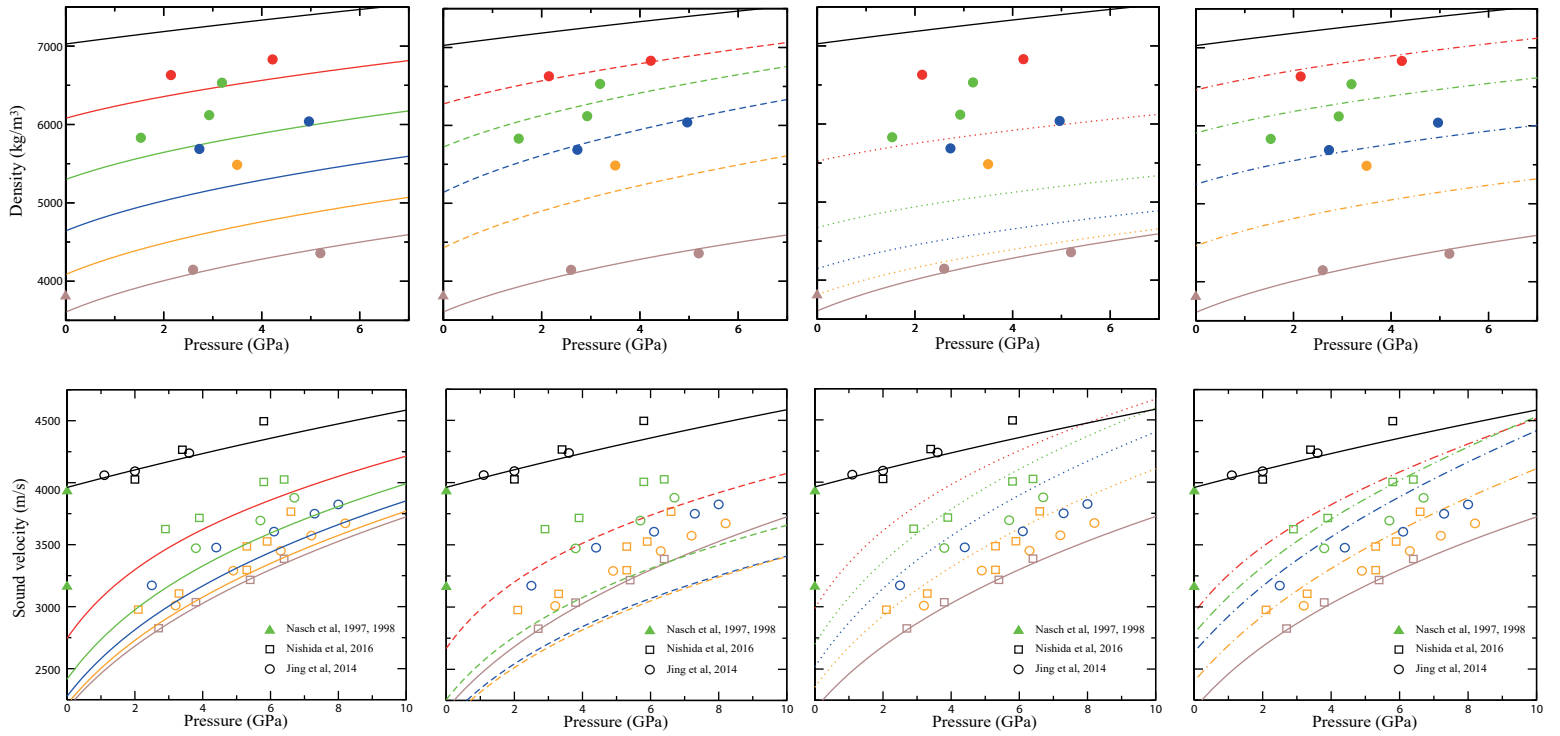


Figure 11

